Title
Direct Measurement of Pyroelectric and Electrocaloric Effects in Thin Films

Journal
Physical Review Applied, 7(3)

ISSN
2331-7043

Authors
Pandya, Shishir
Wilbur, Joshua D
Bhatia, Bikram
et al.

Publication Date
2017-03-01

DOI
10.1103/physrevapplied.7.034025

Peer reviewed

Direct Measurement of Pyroelectric and Electrocaloric Effects in Thin Films

Shishir Pandya,[1] Joshua D. Wilbur,[2] Bikram Bhatia,[3] Anoop R. Damodaran,[1] Christian Monachon,[2] Arvind Dasgupta,[1] William P. King,[4] Chris Dames,[2,5] and Lane W. Martin[1,5,*]

[1]*Materials Science and Engineering, University of California, Berkeley, Berkeley, California 94720, USA*
[2]*Mechanical Engineering, University of California, Berkeley, Berkeley, California 94720, USA*
[3]*Mechanical Engineering, Massachusetts Institute of Technology, Cambridge, Massachusetts 02139, USA*
[4]*Mechanical Science and Engineering, University of Illinois, Urbana-Champaign, Urbana, Illinois 61801, USA*
[5]*Materials Sciences Division, Lawrence Berkeley National Laboratory, Berkeley, California 94720, USA*

(Received 16 December 2016; revised manuscript received 21 February 2017; published 28 March 2017)

An understanding of polarization-heat interactions in pyroelectric and electrocaloric thin-film materials requires that the electrothermal response is reliably characterized. While most work, particularly in electrocalorics, has relied on indirect measurement protocols, here we report a direct technique for measuring both pyroelectric and electrocaloric effects in epitaxial ferroelectric thin films. We demonstrate an electrothermal test platform where localized high-frequency (approximately 1 kHz) periodic heating and highly sensitive thin-film resistance thermometry allow the direct measurement of pyrocurrents (<10 pA) and electrocaloric temperature changes (<2 mK) using the "2-omega" and an adapted "3-omega" technique, respectively. Frequency-domain, phase-sensitive detection permits the extraction of the pyrocurrent from the total current, which is often convoluted by thermally-stimulated currents. The wide-frequency-range measurements employed in this study further show the effect of secondary contributions to pyroelectricity due to the mechanical constraints of the substrate. Similarly, measurement of the electrocaloric effect on the same device in the frequency domain (at approximately 100 kHz) allows for the decoupling of Joule heating from the electrocaloric effect. Using one-dimensional, analytical heat-transport models, the transient temperature profile of the heterostructure is characterized to extract pyroelectric and electrocaloric coefficients.

DOI: 10.1103/PhysRevApplied.7.034025

I. INTRODUCTION

Ferroelectrics possess a spontaneous polarization that is strongly temperature and electric field dependent. The variation of polarization with a changing temperature results in the *pyroelectric effect* (PEE), parametrized by the pyroelectric coefficient, $\pi = (\partial P/\partial T)_E$ [1]. The application of an electric field can also drive changes in the polarization and the *electrocaloric effect* (ECE), where the application or withdrawal of an electric field results in an isothermal entropy $(\partial S/\partial E)_T$ or adiabatic temperature change [2]. Such effects are widely utilized in a range of applications: pyroelectrics for infrared imaging, radiometry, and electron emission [3,4] and for the recovery of electrical energy from waste heat [5,6]; and electrocalorics for environmentally friendly, solid-state cooling technologies (i.e., low-power, gaseous refrigerant-free, etc.) [7,8].

The pyroelectric coefficient π is typically characterized by measuring the pyroelectric current ($i_P = A\pi(dT/dt)$, where A is the area of the capacitor and dT/dt the temperature ramp rate) generated in response to a known temperature transient. Most techniques used to measure pyroelectric properties were developed to probe bulk ceramics or single crystals, including laser-induced heating [9] and continuous ramp-rate heating studies [10]. These techniques are adequate to estimate π for large samples (or large-area capacitors) but lack the precision, as a consequence of poor temperature accuracy, nonuniform heating, and contributions from thermally-stimulated currents due to the release of trapped charges [11,12], to measure small-volume samples (and small-area capacitors) [13]. For all materials, but particularly for thin-film samples, measurement methods that can separate out deleterious or spurious signals are the key to accurately measuring the true pyroelectric nature. In turn, the work on thin films has turned to phase-sensitive pyroelectric measurement techniques [14,15], including those based on microfabricated resistive heater-based measurements [16] and modulated laser-based approaches [17], to more accurately assess the pyroelectric response of these small-volume samples.

The ECE, on the other hand, is parametrized by the isothermal entropy change ($\Delta S_{\text{iso}} = -\int_{E_1}^{E_2} \Sigma dE$), where $\Sigma = (\partial S/\partial E)_T$ is the electrocaloric coefficient. In the case of bulk materials, the traditional approach to measuring this quantity is to measure either the change in temperature using thermometry [18] or the heat flux using calorimetry [19,20]. Similar to the PEE, the past few decades have seen growing interest in investigating the

*lwmartin@berkeley.edu

ECE in thin films, and, in turn, a need for more advanced measurement approaches has developed. Driven by advances in thin-film epitaxy, researchers can now synthesize ferroelectric thin films and superlattices with atomic-level control over composition and epitaxial strain [21,22]. It is thought that such thin-film versions of ferroelectrics can undergo significantly larger (order-of-magnitude) temperature changes, as they can be driven considerably harder than their bulk counterparts owing to the fact that considerably higher fields can be applied to these thin versions of materials [23]. In turn, reports of a large ECE in thin films of $PbZr_{0.95}Ti_{0.05}O_3$ [24], $(1-x)PbMg_yNb_{1-y}O_3-(x)PbTiO_3$ [25,26], and $SrBi_2Ta_2O_9$ [27] have rejuvenated interest in the study of the ECE.

Despite this growing interest, these electrothermal responses (i.e., the PEE and ECE) in thin films remain considerably understudied compared to dielectric, piezoelectric, and ferroelectric effects. This discrepancy in the study (and, in turn, understanding) is primarily related to the fact that direct (and accurate) measurements of the temperature changes are difficult. The small thermal mass of thin-film-based devices and the presence of the substrate lead to nonadiabatic conditions where the film loses heat to the substrate with a time constant smaller than the characteristic time constant for the application (or removal) of the electric field [28]. These inherent difficulties in measurement have, therefore, resulted in the majority of work to date relying on so-called "indirect" methods to measure ECEs. In such indirect approaches, the polarization is measured as a function of the electric field at different temperatures to extract $(\partial P/\partial T)_E$, and the ECE is inferred via the application of the Maxwell relation $(\partial P/\partial T)_{E,\sigma,\text{or}\,\varepsilon}=(\partial S/\partial E)_{T,\sigma,\text{or}\,\varepsilon}$. This allows one to estimate the isothermal dipolar entropy change (ΔS_{iso}) and, in turn, the adiabatic temperature change (ΔT_{ad}) as [2,29], respectively,

$$\Delta S_{\text{iso}}=\int_{E_1}^{E_2}\left(\frac{\partial P}{\partial T}\right)_E dE, \tag{1}$$

$$\Delta T_{\text{ad}}=-\int_{E_1}^{E_2}\left(\frac{T}{C(T,E)}\right)\left(\frac{\partial P}{\partial T}\right)_E dE, \tag{2}$$

where $C(T,E)$ is the volumetric heat capacity. Many recent reports of large ECEs, including $\Delta T=12$ K for $PbZr_{0.95}Ti_{0.05}O_3$ ($\Delta E=480\ \text{kV cm}^{-1}$, initial temperature of 220 °C) [24], $\Delta T\approx 12$ K for the ferroelectric copolymer P(VDF-TrFE) [30], and a colossal $\Delta T=45.3$ K at the transition temperature of films of the relaxor ferroelectric $Pb_{0.8}Ba_{0.2}ZnO_3$ [31], have utilized this indirect approach. The correct application of this approach, however, requires that the appropriate mechanical boundary conditions of the material are considered, particularly in the case of thin films, where the mechanical clamping to the rigid substrate breaks the thermodynamic equivalence of Σ and π [32]. Ultimately, the development of reliable measurement techniques for thin films is needed to truly understand the mechanism and magnitude of these responses and to inspire more confidence for the design of electrocaloric devices.

In this work, we develop an electrothermal test platform to characterize the PEE and ECE in thin films using an adaptation of "2-omega" and "3-omega" techniques, respectively. Traditionally, such 3-omega approaches have been used to measure the thermal conductivity of thin films [33]. For measurements of the PEE, the ferroelectric thin film is locally heated in a periodic fashion via a thin-film, microfabricated heater at frequencies up to approximately 1 kHz, and the resulting current is measured using phase-sensitive detection. Using the 3-omega method, periodic temperature oscillations in the ferroelectric resulting from the periodic heating of the heater line are measured. In turn, by measuring the thermal phase lag in the ferroelectric layer, the thermally-stimulated current (which lags the pyroelectric current by 90°) are separated from the pyroelectric current offering accurate probes of the PEE. The same device can then further be used to measure directly the ECE in thin films. In the ECE measurement, ac electric fields are applied across the ferroelectric capacitor, and the resulting temperature change of the top microfabricated heater (now functioning solely as a temperature sensor) is measured using a modified 3-omega method. Using 1D analytical heat-transport models, the Σ and the average temperature change in the ferroelectric are calculated. The measurement of both the PEE and the ECE on the same device allows us to compare the differences between the two electrothermal effects. Here, we describe the design and fabrication of these electrothermal devices, the underlying physics of the measurements, and the extraction of the physical properties and demonstrate the capabilities of this technique in a model ferroelectric thin film of $PbZr_{0.2}Ti_{0.8}O_3$. We show that pyrocurrents <10 pA and temperature changes <2 mK can be reliably measured allowing us to characterize micron-scale, thin-film (approximately 100 nm) devices with an extremely small thermal mass (approximately 6×10^{-9} g).

II. DEVICE DESIGN

Measurement of both the PEE and the ECE on the same thin-film heterostructure requires the ability to (i) heat the ferroelectric thin film and measure i_P flowing across the ferroelectric in a capacitor circuit and (ii) apply electric fields across the ferroelectric and measure the temperature change in the ferroelectric layer. This calls for an independent ferroelectric circuit, comprised of a rectangular capacitorlike geometry with symmetric top and bottom electrodes, and a thermal circuit, comprised of a narrow thin-film metal strip acting as a heater wire and four-point probes for thermal sensing.

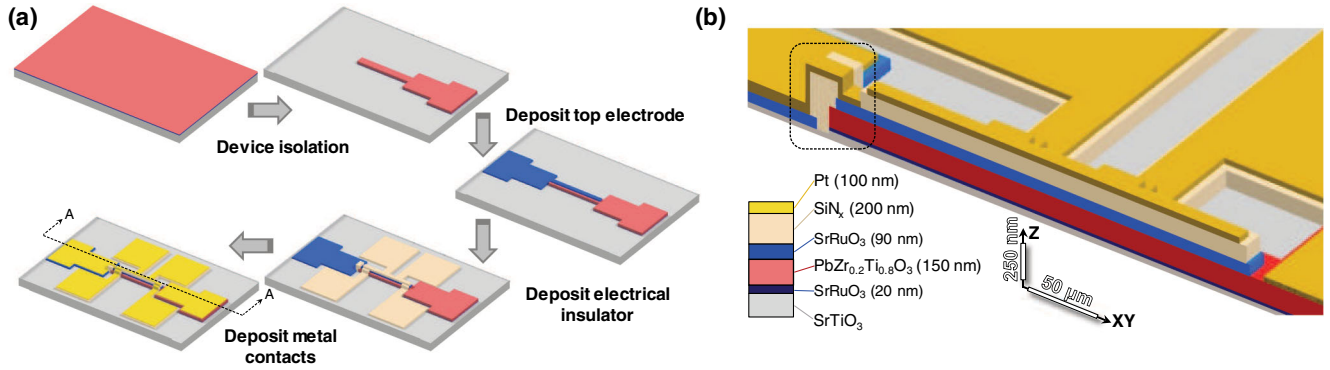

FIG. 1. (a) Schematic of the process to fabricate the electrothermal device for measuring pyroelectric and electrocaloric effects in thin films. (b) Section view through the view *A*-*A* depicting various layers in the heterostructure. The film under test here is $PbZr_{0.2}Ti_{0.8}O_3$ (red), while the top and the bottom $SrRuO_3$ layers (blue and dark blue, respectively) connect to the top and bottom metal contacts.

Here, as a demonstration of the potential of this approach, we focus on measuring the electrothermal response of a 150-nm-thick thin film of $PbZr_{0.2}Ti_{0.8}O_3$ epitaxially grown on 20-nm-thick $SrRuO_3/SrTiO_3$ (001) substrate via pulsed-laser deposition using established processes [34]. Following growth, the electrothermal characterization devices are produced via a multistep, microfabrication process. Briefly, the ferroelectric heterostructure is lithographically patterned and ion-milled to define the bottom electrode and the ferroelectric "active" layer [Fig. 1(a)]. This step removes the bottom electrode ($SrRuO_3$) everywhere except under the active layer and the bottom electrode probe pad. This greatly reduces the risk of electrical shorting of the top and the bottom electrode during wire bonding. In this work, 90 nm $SrRuO_3$ is then selectively deposited as a symmetric top electrode using a MgO hard-mask process [35] to establish a rectangular ferroelectric capacitor geometry ($300\ \mu m \times 20\ \mu m$). It should be noted that the $SrRuO_3$ deposited over the ferroelectric or bottom-electrode mesa does not contact the $SrRuO_3$ deposited on the ion-milled region of the substrate to be used later for establishing an electrical contact pad. This is done purposefully to ensure that the $SrRuO_3$ does not get deposited on the sidewalls of the ferroelectric layer and electrically short to the bottom electrode. Next, to electrically isolate this ferroelectric circuit from the thermal circuit, a 200-nm-thick blanket layer of SiN_x is deposited using plasma-enhanced chemical vapor deposition ($SiH_4 + NH_3$ based). SiN_x is chosen as it exhibits a low dielectric constant (approximately 7) and a thermal conductivity of 2 $Wm^{-1}K^{-1}$ measured via the differential 3-omega method [33]. The deposition temperature of the nitride is limited to 350 °C to limit decomposition (i.e., Pb, Ru, or O loss) of the films. This nitride layer is subsequently patterned and selectively etched using reactive ion etching in a SF_6 plasma, to obtain an electrically insulating film on top of the ferroelectric capacitor. Etching the SiN_x from everywhere around the ferroelectric capacitor reduces the lateral dissipation of heat, which makes the top sensor line more sensitive to measuring small temperature changes. Finally, a 100-nm-thick platinum thin-film resistance heater and thermometer is lithographically patterned in the shape of a thin strip with four probe pads [two outer and two inner pads; see the geometry in Fig. 1(a)] to define the thermal circuit [Fig. 1(b)]. Platinum contact pads for the top and the bottom electrode are also

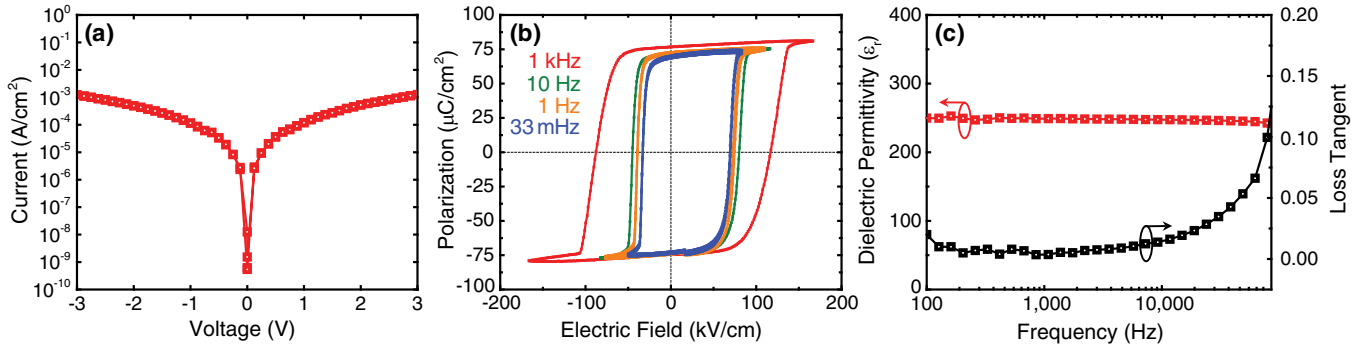

FIG. 2. (a) dc current-voltage characteristics, (b) ferroelectric hysteresis loops, and (c) dielectric permittivity and loss tangent as a function of the frequency for a 150-nm-thick $PbZr_{0.2}Ti_{0.8}O_3$ device obtained at 300 K.

defined in this step. While the platinum pad for the bottom electrode contacts the bottom $SrRuO_3$ as the device gets wire bonded, the platinum pad for the top electrode contact runs over the SiN_x to contact the top $SrRuO_3$ without shorting with the bottom electrode [see the highlighted region in Fig. 1(b)].

Prior to any electrothermal measurements, we investigate the room-temperature current-voltage, ferroelectric, and dielectric response of the thin-film heterostructures. Current-voltage measurements reveal that the devices exhibit a symmetric and highly-resistive response ($R_{FE} > 10^8\ \Omega$) and that the electrode contacts are rectifying [36], altogether confirming the high-quality, low-leakage characteristics of the heterostructures [Fig. 2(a)]. Ferroelectric hysteresis loops are measured between 0.033 and 1000 Hz [Fig. 2(b)], and the devices exhibit a robust ferroelectric response with low-loss, square ferroelectric hysteresis loops, large remnant polarization ($P_r \approx 77\ \mu C/cm^2$), and loop closure even at the lowest measurement frequencies, again confirming the excellent quality of the ferroelectric films and devices. Low-field dielectric permittivity measurements are also conducted on the same devices [Fig. 2(c)]. A near-frequency-independent value of the dielectric permittivity (approximately 248 ± 2.7) is measured across the frequency range of 10^2–10^5 Hz at room temperature, consistent with expectations for these heterostructures [37].

III. THEORY OF MEASUREMENTS

A. Pyroelectric effect

The pyroelectric measurement [Fig. 3(a)] relies on the application of a sinusoidally varying current $[I_{H,1\omega_H} = I_{0H}\cos(\omega_H t)]$ at frequency ω_H across the outer thermal-probe pads. The driving current at frequency ω_H dissipates power equal to $I^2_{H,1\omega_H}R_0 = \frac{1}{2}I^2_{0H}[1 + \cos(2\omega_H t)]$, where R_0 is the resistance of the heater line (approximately 30 Ω). Because the response in the thermal domain is linear, periodic Joule heating causes temperature oscillations with ac amplitude θ_H at $2\omega_H$ [Fig. 3(b)]. For a simple heater-on-substrate geometry, the heat generated in the top metal heater line diffuses into the substrate a characteristic distance (often referred to as the penetration depth or thermal wavelength) defined as [38]

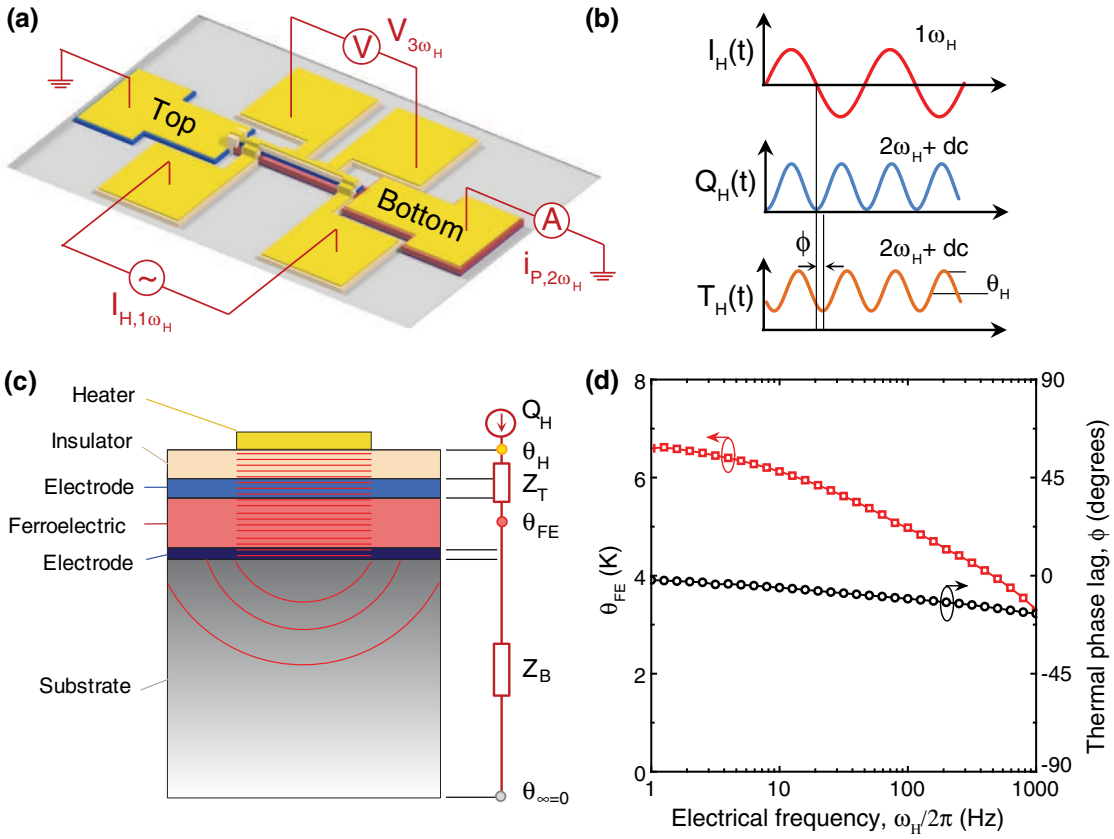

FIG. 3. (a) Schematic of the setup for pyroelectric and 3-omega measurement. (b) Schematic of the relationship between the applied heating current $[I_H(t)]$ at angular frequency $1\omega_H$, dissipated power $[Q_H(t)]$, and the resulting temperature oscillation $[T_H(t)]$ of the metal heater line at $2\omega_H$. (c) Schematic of the temperature field during a pyroelectric measurement and a simplified thermal circuit. (d) Measured temperature oscillation θ_{FE} and thermal phase lag ϕ between the heating current (and, therefore, the dissipated power) and the temperature change in the ferroelectric as a function of the frequency.

$$\lambda_S = \sqrt{\frac{D_S}{2\omega_H}}, \tag{3}$$

where D_S is the thermal diffusivity of the substrate.

To calculate the ac amplitude of the temperature oscillation in the ferroelectric thin film (θ_{FE}), first the amplitude of the temperature change in the heater line (θ_H) is measured using the 3-omega method [33]. The heating frequency is chosen so that the heat completely propagates through the film stack while still ensuring that the substrate remains semi-infinite such that the thermal waves completely dampen within the substrate [Fig. 3(c)]. Thus, the natural bounds on the thermal wavelength are $\lambda_{\mathrm{FE}} > 3d_{\mathrm{FE}}$ and $\lambda_S < \frac{1}{3}d_S$, where the subscripts FE and S denote the ferroelectric film and substrate, respectively, and d is the thickness of the relevant component. Key to the sensitivity and accuracy of this approach is the fact that the thermal impedance of the top thermal circuit Z_T (comprising the heater line, the electrical insulator, and the top oxide-metal electrode) is much smaller than that of the bottom circuit Z_B (comprising the bottom oxide-metal electrode and the substrate), thereby minimizing the error between θ_H and θ_{FE}. The amplitude and phase (ϕ) of the temperature oscillation of the heater line depend upon the thermal properties of the system (i.e., the thermal conductivity and specific heat capacity) and are measured using the 3-omega method.

The measured θ_H and the thermal flux (q_H) into the heterostructure (i.e., the ac power dissipated per unit area of the heater) are used with a one-dimensional thermal transport model [39] to calculate θ_{FE} (see the Appendix for details). This scheme is applied to calculate θ_{FE} at five equally spaced nodes within the ferroelectric layer. We find that the difference in the temperature amplitude between the top (just below the ferroelectric and top electrode interface) and bottom nodes (just above the ferroelectric and bottom electrode interface) corresponds to 1.6% of the average θ_{FE}. Hence, any tertiary PEE [40] induced by temperature gradients in the film can be neglected, and we can use the lumped parameter approach where the ferroelectric layer is considered to be isothermal at any instant. A similar approach [16] calculates θ_{FE} using q_H and works from the bottom of the substrate up to the ferroelectric layer. We, however, choose to work from the top down so as to maximize the number of measured quantities in the model to compensate for any unideal deviation from the theory.

The mean temperature oscillation of the ferroelectric, averaged across the five nodes, θ_{FE}, as a function of the frequency is thus extracted and plotted [Fig. 3(d)]. It can be seen that θ_{FE} decreases and the phase between the dissipated power (as a result of heating) and the temperature (ϕ) increasingly lags as the frequency of the ac heating current on the top metal line increases [Fig. 3(d)]. The phase lag behaves as expected, approaching 0° and −17.5° in the low- and high-frequency limits, respectively, reflecting the gradual transition from cylindrical to one-dimensional heat transport. Determination of the thermal phase lag is particularly important for extracting i_P, which can be convoluted with thermally-stimulated currents that are in phase with the temperature change.

With the known thermal state of the heterostructure in response to periodic Joule heating, we can proceed to extract i_P and π. The current is measured through the bottom electrode using the current input (10^6 V/A gain) of a lock-in amplifier (Stanford Research, SR830) [Fig. 3(a)]. The top electrode is held at the ground potential, which shields any capacitive coupling between the heating and the ferroelectric measurement circuits. Since i_P is proportional to the rate of change of the temperature, it leads the temperature change by 90° and is extracted by taking the component of the measured total current which is out of phase (leads by 90°) with the temperature change [14,15]. Thereafter, π can be calculated using the formula $i_P = A\pi(dT/dt)$.

B. Electrocaloric effect

Measuring the ECE relies on the ability to sense small temperature changes when an electric field is applied and removed across the ferroelectric. A sinusoidally varying electric field $E = (V_0/d_{\mathrm{FE}})\sin(\omega_E t)$, when applied to the bottom electrode of the ferroelectric capacitor as depicted [Fig. 4(a)], results in an adiabatic temperature change via the ECE:

$$\Delta T_{\mathrm{ad}} = -\int_{E_1}^{E_2}\left(\frac{T}{C(T,E)}\right)_E \Sigma dE. \tag{4}$$

The temperature change via the ECE, unlike the case of Joule heating which happens at dc and 2ω, happens at ω. This can be understood by calculating the ECE power (Q_E):

$$Q_E = C(T,E)Ad_{\mathrm{FE}}\frac{dT}{dt}, \tag{5}$$

where A is the area of the heat source (ferroelectric layer). Using Eq. (4), Eq. (5) can be simplified to

$$Q_E = -T\Sigma A\omega_E V_{0E}\cos(\omega_E t). \tag{6}$$

Hence, the electrocaloric power and the resultant temperature change occur at the same frequency, ω_E [Fig. 4(b)]. Power dissipation due to Joule heating, on the other hand, is given by

$$Q_J = \frac{V_{0E}^2}{2R_{\mathrm{FE}}}[1-\cos(2\omega_E t)], \tag{7}$$

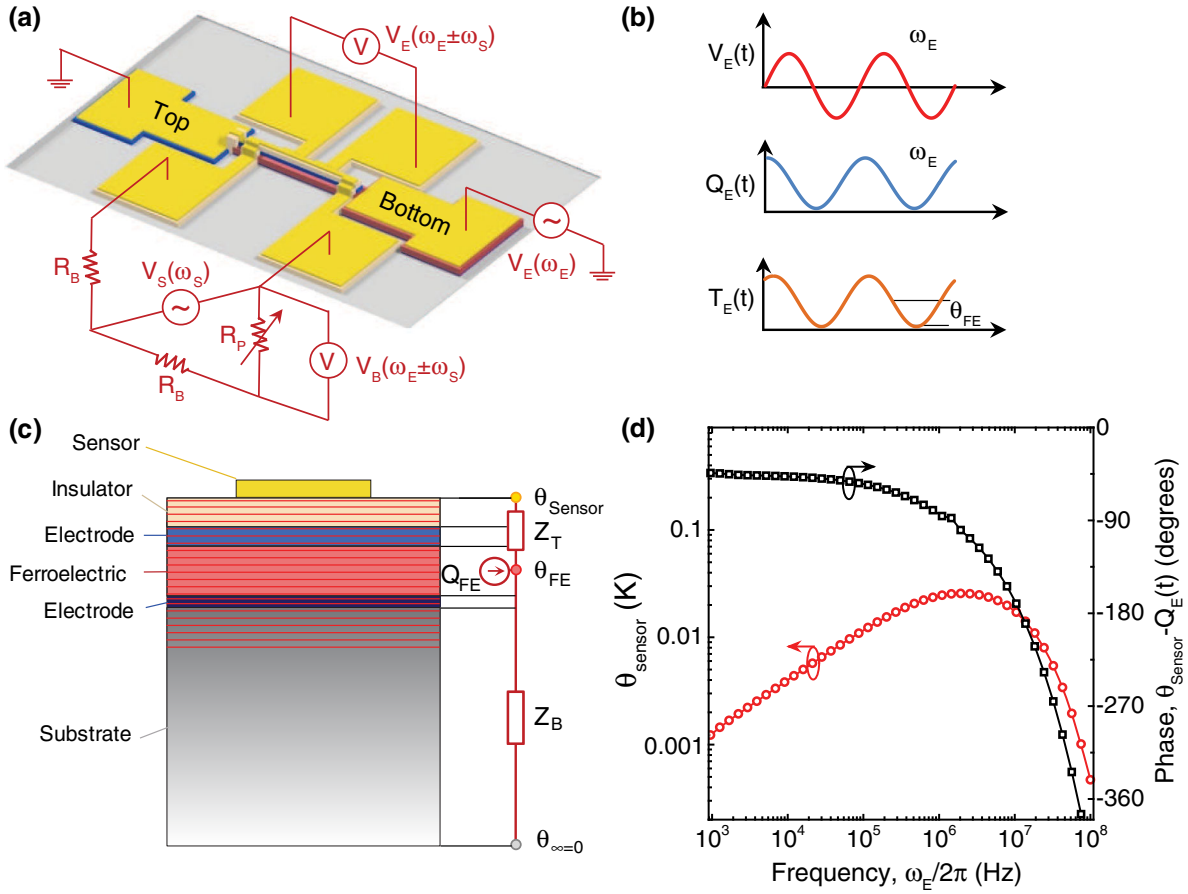

FIG. 4. (a) Schematic of the setup for electrocaloric measurement using the top metal line as a resistance thermometer (sensor). (b) Schematic of the relationship between the applied voltage $[V_E(t)]$ across the ferroelectric capacitor at angular frequency ω_E, the power generated $[Q_E(t)]$, and the resulting temperature change $[T_E(t)]$ due to the ECE at the same frequency ω_E. (c) Schematic of the temperature field during an electrocaloric measurement. (d) Computed temperature oscillation θ_{sensor} and thermal phase lag between the temperature oscillation of the top sensing metal line and the ECE power as a function of the frequency of voltage cycling across the ferroelectric for an assumed $\Sigma = -100\ \mu\text{Cm}^{-2}\ \text{K}^{-1}$ and an applied electric-field amplitude of 50 kV cm^{-1}.

where R_{FE} is the resistance of the ferroelectric. Thus, Joule heating still happens at dc and $2\omega_E$, thereby making ECE measurements in the frequency domain at ω_E effective in filtering out contributions from Joule heating.

The temperature oscillation of the top sensor line (θ_{sensor}) can be related to the ECE power from the underlying ferroelectric film (Q_E) via a generic thermal transfer function in the frequency domain, Z [41]:

$$\theta_{\text{sensor}}(t) = Q_{0E}[\text{Re}(Z)\cos(\omega_E t) + \text{Im}(Z)\sin(\omega_E t)], \quad (8)$$

where $Q_{0E} = -T\Sigma A\omega_E V_{0E}$ from Eq. (6). This temperature change perturbs the electrical resistance of the top metal heater or sensor line as

$$R_{\text{sensor}} = R_{0,\text{sensor}}[1 + \alpha\Delta T_{\text{dc}} + \alpha\theta_{\text{sensor}}], \quad (9)$$

where $R_{0,\text{sensor}}$ is the resistance of the sensor line at 300 K (approximately 10 Ω) and α is the temperature coefficient of resistance. To sense the temperature in the top metal line, a sensing signal of the form $V_S\sin(\omega_S t)$ is applied across the outer thermal pads [Fig. 4(a)]. The voltage source is converted to a current source by the inclusion of a ballast resistor (R_B, which is 10^2 times larger than R_{sensor}) in series. Other approaches include the use of a commercially available ac current source (for example, Keithley 6221A) or a custom-built V-to-I circuit using operational amplifiers [42]. Voltage (V_A) is measured across the inner pads of the thermometer and has the form

$$V_A = \frac{V_S\sin(\omega_S t)}{R_B + R_{\text{sensor}}}R_{\text{sensor}}. \quad (10)$$

Since $(R_B/R_{\text{sensor}}) \geq 10^2$, using Eqs. (8) and (9), Eq. (10) can be expressed as

$$V_A = \frac{V_S\sin(\omega_S t)}{R_B} \times R_{\text{sensor}}\{1 + \alpha\Delta T_{\text{dc}} + \alpha Q_{0E}[\text{Re}(Z)\cos(\omega_E t) + \text{Im}(Z)\sin(\omega_E t)]\}. \quad (11)$$

The response frequencies $\omega_S \pm \omega_E$ (due to the product of two sinusoidal functions) contain the information regarding the temperature oscillation of the sensor. The voltage signal corresponding to ω_S is particularly large and can be 1000 times larger than the one corresponding to $\omega_S \pm \omega_E$, resulting in a significantly larger background. Therefore, a common mode-cancellation circuit using a Wheatstone bridge is implemented in our measurement scheme [Fig. 4(a)]. The sensing signal is simultaneously applied across a potentiometer, which is adjusted such that the resistance of the potentiometer $R_P \approx R_{0,\text{sensor}}$ and, therefore, the voltage drop (V_B) across R_P nullifies the ω_S component of the differential voltage ($V_A - V_B$) that is fed to the lock-in amplifier. Note that the $\omega_S \pm \omega_E$ signal comes only from the temperature-dependent response due to the ECE (R_{sensor}) and is absent in the potentiometer (R_P). Therefore, only the ω_S background is attenuated, and the measurement of the much smaller $\omega_S \pm \omega_E$ signal becomes possible.

The measured differential voltage ($V_{\omega_S \pm \omega_E}$) is related to the temperature oscillation of the top sensor via [43,44]

$$\theta_{\text{sensor}} = 2\frac{1}{\alpha V_{\omega_S}} V_{\omega_S \pm \omega_E}. \quad (12)$$

This temperature change of the top sensor line is used to calculate Σ as well as the average temperature oscillation in the ferroelectric, θ_{FE}. This requires knowledge of the volumetric power generation (G) created by the entropy change and can be related to Σ as [32]

$$G = -T\frac{dS}{dE}\frac{dE}{dt} = -T\Sigma\left(\frac{V_{0E}}{d_{\text{FE}}}\right)\omega_E \cos(\omega_E t). \quad (13)$$

The resulting heat flux can be determined from the measured temperature change on the top sensor line and the thermal properties of all the layers in the heterostructure. Because of the ECE, heat flux is generated homogeneously in the ferroelectric and diffuses in both directions (i.e., into the substrate and into the top sensor line). To model this heat transport, we solve a 1D problem for the heat flux generated in each differential thickness (dz) at a height z in the ferroelectric [32]. We define G to be the power generated per unit volume and note that the differential flux dq_{tot} generated from each volume is $dq_{\text{tot}} = G dz$. The total temperature oscillation sensed by the metal sensor is the sum of the contributions from the entire thickness of the ferroelectric [Fig. 4(c)]. This is a continuous domain, so summation is replaced by integration and the amplitude of the temperature oscillations sensed by the metal line is defined by

$$\theta_{\text{sensor}} = G\int_0^{d_{\text{FE}}} \xi dz, \quad (14)$$

where ξ is an algebraic expression calculated using the elements of the thermal transport matrices and the appropriate boundary conditions (see the Appendix for details). Using Eq. (13), Eq. (14) simplifies to

$$\theta_{\text{sensor}} = -T\Sigma\left(\frac{V_{0E}}{d_{\text{FE}}}\right)\omega_E \cos(\omega_E t)\int_0^{d_{\text{FE}}} \xi dz. \quad (15)$$

Equation (15) allows the calculation of Σ from the measured value of θ_{sensor}. Furthermore, the average temperature oscillations of the ferroelectric, θ_{FE}, can be calculated using a similar approach to find the temperature amplitudes at the top and bottom surface of the ferroelectric and then taking their average.

In our measurements, high-frequency electric-field oscillations are required to generate enough flux to produce a measurable temperature change. The effect of the driving frequency on the resulting temperature change on the top sensor line, for an assumed $\Sigma = -100\ \mu\text{C m}^{-2}\text{K}^{-1}$ and an applied electric-field oscillation of 50 kV cm^{-1}, is calculated from the above thermal models and shown for reference [Fig. 4(d)]. It can be seen that, at lower frequencies ($<3 \times 10^6$ Hz), the temperature change on the top metal sensor is limited due to low thermal flux [refer to Eq. (15)]. At high frequencies ($>3 \times 10^6$ Hz), the temperature change diminishes due to the limited thermal penetration depth, placing an upper limit on the frequency range of the experiment. It is therefore desirable to perform ECE measurements at frequencies in the range close to 2×10^5–1×10^6 Hz.

IV. RESULTS AND DISCUSSION

A. Pyroelectric effect

Following the theory of pyroelectric measurement in Sec. III A (Fig. 3), the power spectrum of the measured total current (i_{total}) is provided [Fig. 5(a)] for a heating current ($I_{H,1\omega_H}$) equal to 16 mA at 1 kHz. It can be seen that a dominant current peak occurs at frequency $2\omega_H$ as a result of the temperature oscillations at the same frequency in the ferroelectric due to the driving current at $1\omega_H$ in the heater line [inset, Fig. 5(a)]. It should be noted that the presence of the electrically insulating SiN_x layer and electrical shielding via the top electrode reduces, but does not completely suppress, the capacitive coupling. This manifests as the observed response at ω_H [Fig. 5(a)]; however, our ability to measure i_P (measured at $2\omega_H$ frequency) is not affected by the nonzero capacitive coupling. The basis of this argument is twofold. First, measurements with zero heating, but with capacitive bias across the heterostructure, yield 2ω current which is approximately 10^3 smaller than the case when heating occurs in conjunction with the capacitive bias. Second, we measure the total current with the polarization of the ferroelectric in the up-poled state (i_{up}) and the down-poled state (i_{down}). Since the switching of the polarization only reverses the direction of i_P (manifested as a phase

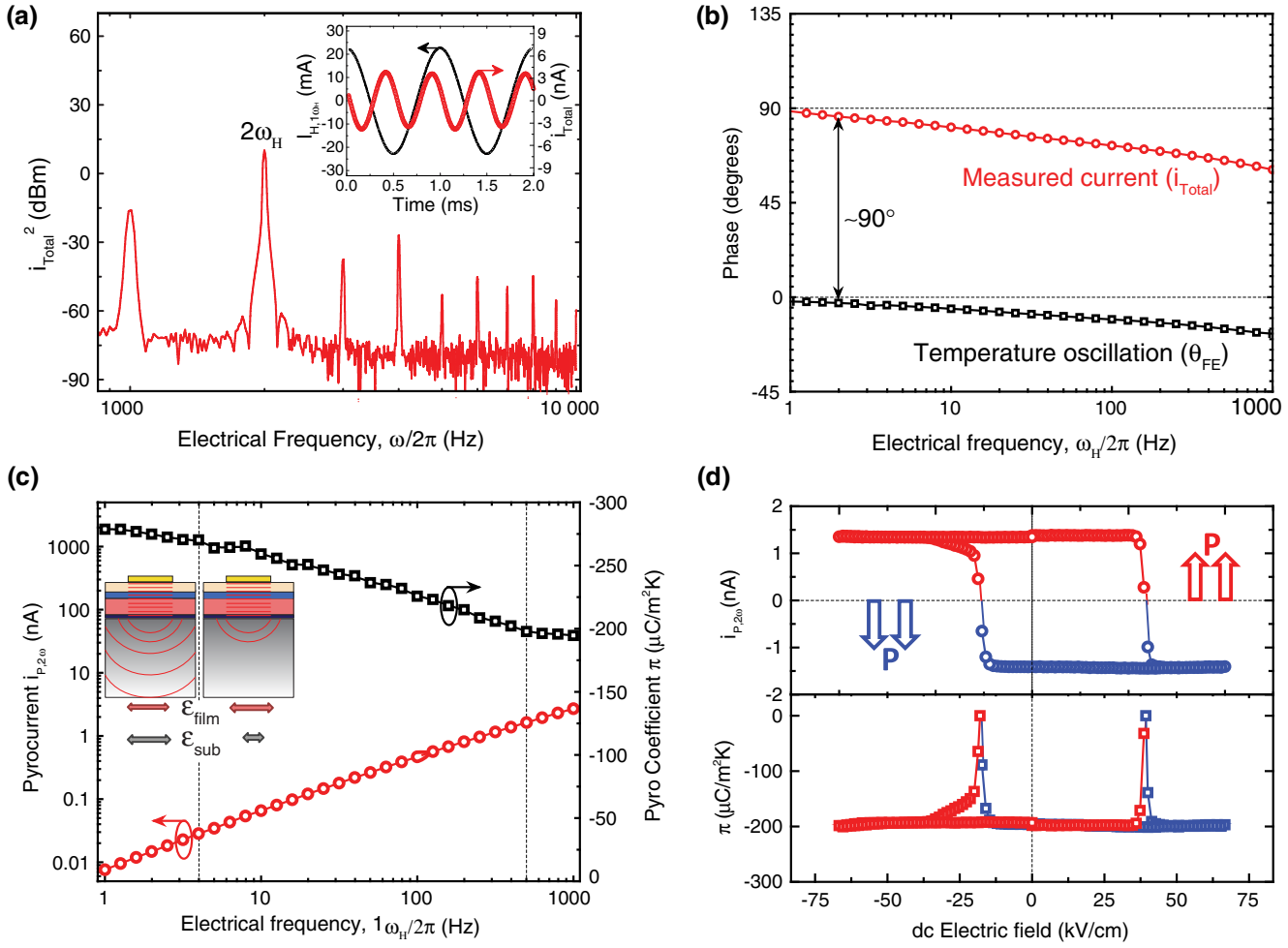

FIG. 5. Pyroelectric measurements of $PbZr_{0.2}Ti_{0.8}O_3$ thin film. (a) Measured total current (i_{total}) in the frequency domain and time domain (inset) for an applied heating current ($I_{H,1\omega_H}$) equal to 16 mA at a frequency of 1 kHz. (b) Phase relationship of the measured current (at $2\omega_H$) and the temperature oscillation (also at $2\omega_H$) with respect to the phase of the applied heating current depicting that the measured current leads the temperature oscillation by approximately 90°. (c) Measured pyroelectric current and pyroelectric coefficient as a function of the heating frequency. At low frequencies (<4 Hz), $\pi \to (\partial P/\partial T)_{E,\sigma}$, while at high frequencies (>500 Hz), $\pi \to (\partial P/\partial T)_{E,\varepsilon}$ due to the secondary contribution to pyroelectricity (reduction by approximately 30%). (d) Pyroelectric hysteresis loops as a function of the background dc electric field, at 1 kHz.

reversal by 180°) and does not change the capacitively coupled parasitic current, i_{up} and i_{down} can be expressed as

$$i_{up} = i_P + i_{parasitic}, \tag{16}$$

$$i_{down} = -i_P + i_{parasitic}. \tag{17}$$

By taking the sum and difference of Eqs. (16) and (17), we are able to subtract out any contribution due to parasitic coupling, which constitutes less than 4% of the total measured current. These two checks confirm that the current due to parasitic capacitance is negligible. This, however, does not prove that the current is completely pyroelectric in origin. Our measurements show that the measured current leads the actual temperature change in the ferroelectric [Fig. 3(d)] by approximately 90° [Fig. 5(b)]. Deviations from the expected phase can be attributed to thermally-stimulated currents which flow in phase (zero lag) with the temperature change. The real i_P is extracted by taking the component of the total current which is out of phase with the temperature change and is plotted as a function of the frequency of heating current [red circles, Fig. 5(c)]. Apparently, π has a frequency dependence [black squares, Fig. 5(c)]. At low frequencies (<4 Hz), π is seen to begin to converge to a value of approximately $-280\ \mu Cm^{-2}\,K^{-1}$, while at higher frequencies (>500 Hz), it asymptotes to a lower value of approximately $-195\ \mu Cm^{-2}\,K^{-1}$. This reduction (approximately 30%) can be explained by the secondary contribution [45] to the total pyroelectricity due to the thermal expansion mismatch between the film and substrate and the resulting thermal-stress-induced, piezoelectric-driven polarization

change. At a low frequency, the thermal penetration depth (λ_S) is large compared to the lateral dimensions of the device; therefore, the ferroelectric film expands and contracts in plane with the substrate. As a result, the total π under a constant stress boundary condition can be expressed as

$$\pi = \left(\frac{\partial P}{\partial T}\right)_{E,\sigma} = \left(\frac{\partial P}{\partial T}\right)_{E,\varepsilon} + \left(\frac{\partial P}{\partial \sigma}\right)_{E,T}\left(\frac{\partial \sigma}{\partial \varepsilon}\right)_{E,T}\left(\frac{\partial \varepsilon}{\partial T}\right)_{E,\sigma}. \tag{18}$$

At higher frequencies, the lateral dimensions of the film do not change as the film is clamped to the substrate, which cannot expand laterally due to the reduced thermal penetration depth. Therefore, the contribution from the lateral thermal expansion $(\partial P/\partial\sigma)_{E,T}(\partial\sigma/\partial\varepsilon)_{E,T}(\partial\varepsilon/\partial T)_{E,\sigma}$ is suppressed, and the magnitude of π decreases.

Changes in the temperature not only change the permanent dipole moment (intrinsic portion of primary pyroelectricity) but also alter the dielectric permittivity and, hence, the surface charge density under an applied electric field. Particularly near a dielectric anomaly (for example, near a phase transition), the dielectric constant changes sharply with the temperature and can result in either a significant suppression or an enhancement of i_P depending upon the poled state of the ferroelectric. The full characterization of π therefore requires one to measure i_P as a function of the background electric field. In our measurements, this is achieved by applying a constant bias voltage to the top electrode while the bottom electrode remains connected to the input of the lock-in amplifier. The measured pyroelectric hysteresis loops are provided [Fig. 5(d)]. When the ferroelectric is up-poled, increasing the temperature results in a "positive" i_P [red data, Fig. 5(d)]. With an increasing positive bias (greater than the coercive field) on the top electrode, the polarization switches and causes i_P to reverse its direction [blue data, Fig. 5(d)]. When the direction of the electric-field bias is reversed (i.e., a negative bias greater than the coercive field is applied), the polarization switches back and i_P reverses direction again, giving a characteristic hysteresislike pyroelectric loop. It should be noted that the slope of i_P vs the electric field is close to zero away from the switching near the coercive fields, indicating that the contribution from the temperature-dependent dielectric permittivity is negligible as the dielectric permittivity does not change strongly with the temperature far from the transition temperature ($T_C > 450\,°\mathrm{C}$).

B. Electrocaloric effect

Measurements are performed on the same device on which the pyroelectric measurements are conducted. The frequency (ω_E) of the applied electric field of magnitude $(V_{0E}/d_{\mathrm{FE}}) = 50\ \mathrm{kV\,cm^{-1}}$ is chosen to be 98 147 Hz, while that of the sensing voltage (ω_S) is chosen to be 2317 Hz with a magnitude $V_S = 7.07$ V. The choice of frequency is determined so as to avoid any resonance between the signal to be measured and power supply noise (harmonics of 60 Hz) or any higher-order harmonics of the sensing signal frequency. A full frequency-domain voltage response is plotted [Fig. 6(a)]. As discussed above, the ECE response in the frequency domain occurs at $\omega_S - \omega_E$ and $\omega_S + \omega_E$ corresponding to 95 830 and 100 464 Hz, respectively. This can be clearly seen against the low background [insets, Fig. 6(a)]. To further validate our technique, we perform the same measurement with varying magnitudes of the applied electric field. We note that the magnitude of the maximum electric field never exceeds the coercive field of switching for the ferroelectric, so that the ECE response (change in temperature) remains linear with the applied electric field [refer to Eq. (15)]. The average temperature change in the ferroelectric layer is found to scale linearly with the applied electric field [red squares,

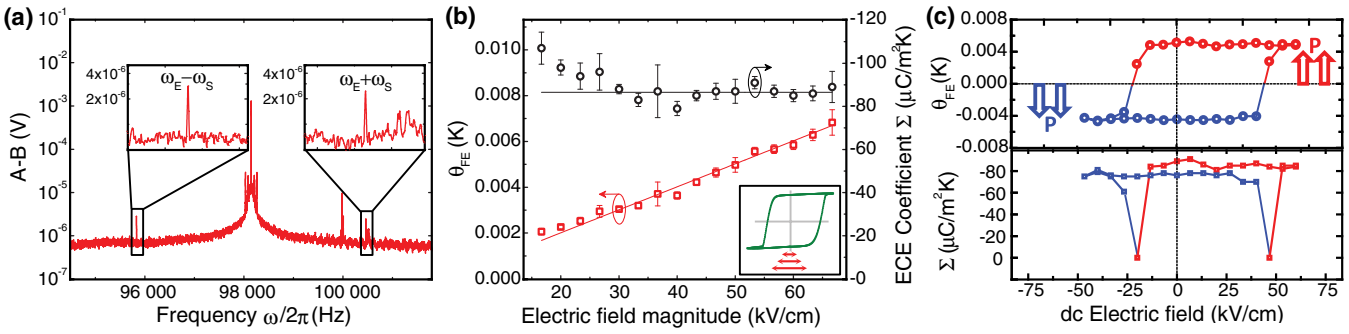

FIG. 6. Electrocaloric measurements of $PbZr_{0.2}Ti_{0.8}O_3$ thin film. (a) Measured differential voltage across the top metal sensor in the frequency domain for an applied electric field of magnitude 50 $\mathrm{kV\,cm^{-1}}$ at a frequency $\omega_E/2\pi$ equal to 98 147 Hz and a sensing voltage V_S equal to 7.07 V at a frequency $\omega_S/2\pi$ equal to 2317 Hz. The inset shows the voltage response at frequency $\omega_S - \omega_E$ and $\omega_S + \omega_E$, which is a measure of the change in the resistance and thus θ_{sensor} of the top metal. (b) Average measured temperature oscillation in the ferroelectric (θ_{FE}) due to the ECE and the resulting calculated value of Σ. (c) Electrocaloric loops as a function of the background dc electric field using an ac electric-field amplitude of 50 $\mathrm{kV\,cm^{-1}}$. The up-poled state (red) results in the positive ECE, while the down-poled state (blue) results in the negative ECE.

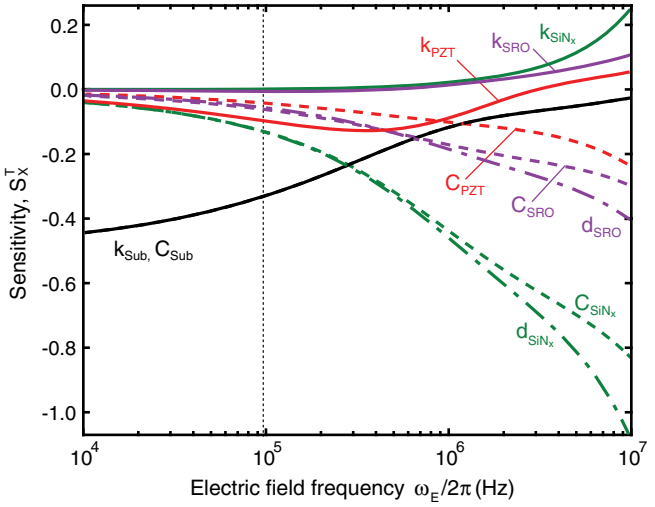

FIG. 7. Sensitivity of the calculated electrocaloric temperature change at the top metal sensor, θ_{sensor}, as a function of the selected parameters in the thermal model as a function of the frequency of electric-field cycling for a 150-nm $PbZr_{0.2}Ti_{0.8}O_3$ heterostructure. The dashed line denotes the frequency of electric-field cycling employed for the electrocaloric experiments.

Fig. 6(b)]. While frequency-selective measurements at $\omega_S \pm \omega_E$ inherently remove any Joule heating that happens at $\omega_S \pm 2\omega_E$, this measurement additionally proves that the ECE response is free from Joule heating, which would have caused θ_{FE} to scale quadratically with the driving electric field. Using the thermal transport model explained above, Σ is extracted from the measured temperature change of the top metal sensor line [black circles, Fig. 6(b)]. A near-field-independent value of Σ is calculated, further proving the linearity of the response in the electric-field regime without any polarization switching. We do observe slight deviations at a very low magnitude of the electric field which correspond to a low signal-to-noise ratio.

We further measure the ECE response as a function of the background dc electric field [Fig. 6(c)], and, similar to the PEE, a hysteresislike ECE loop is measured. A positive ECE is the increase (decrease) in the temperature of the material when an electric field is applied (removed). This is often the case in dielectrics or ferroelectrics above the Curie temperature. Tetragonal ferroelectrics such as $PbZr_{0.2}Ti_{0.8}O_3$ below the Curie temperature, however, can exist in either of two stable polarization states. It is the relative direction of the polarization vector and the electric-field vector that determines the nature (whether positive or negative) of the ECE. When the ferroelectric is up-poled, applying an electric field parallel to the direction of polarization such that the application of a field further reinforces the electrical dipoles results in a positive ECE [red data, Fig. 6(c)]. The application of a negative electric field greater than the coercive field results in polarization switching. In this down-polarized state, the positive electric-field excitation (which is now antiparallel to the direction of polarization) tends to misalign the dipoles, thereby increasing the dipolar entropy and hence decreasing the temperature. In this regime, the ECE is negative [blue data, Fig. 6(c)]. It is worth mentioning that Joule heating, which under a zero background electric field occurs only at dc and $2\omega_E$, has a component at ω_E under a finite background electric field:

$$Q_J = \left(\frac{V_{0E}^2}{2R_{\text{FE}}} + \frac{V_{\text{dc}}^2}{R_{\text{FE}}}\right) + \frac{2V_{0E}V_{\text{dc}}}{R_{\text{FE}}}\sin(\omega_E t) - \frac{V_{0E}^2}{2R_{\text{FE}}}\cos(2\omega_E). \tag{19}$$

Should Joule heating be significant, the measured voltage response at $\omega_S \pm \omega_E$ will have contributions from Joule heating, the shape of the ECE loop will no longer be squarelike, and the otherwise constant temperature change and Σ (zero slope) exhibit a finite slope [proportional to $(2V_{0E}/R_{\text{FE}})$] with an increasing temperature change with an applied background electric field. Our data [in Fig. 6(c)] do not show any measurable slope under the background electric field, suggesting a highly insulating device as suggested by the measured electrical properties (Fig. 2).

V. SENSITIVITY OF THE MEASUREMENT

The thermal model used for the PEE measurements is not sensitive to any material parameter due to the thin layers and low frequencies. Instead, the predominant error in the calculation of the average temperature change in the ferroelectric comes from the calculation of the heater temperature from the 3-omega equations.

To evaluate the accuracy of the ECE measurement due to the propagation of errors from the various thermophysical properties, we quantify the sensitivity of the measured temperature response of the top metal line sensor (during ECE measurement) in the thermal model as [46]

$$S_x^T = \frac{\partial \ln \theta}{\partial \ln x}, \tag{20}$$

where x is one of the parameters (e.g., thermal conductivity, specific heat capacity, or thickness of a particular layer) in the thermal model. With this definition of sensitivity, a value of $S = -0.1$, for example, means that a 10% increase in parameter x will result in a 1% decrease in θ. Equation (20) is evaluated for the following layer properties: thermal conductivity k, volumetric heat capacity C, and layer thickness d as a function of the frequency (Fig. 7). At low frequencies ($<3 \times 10^5$ Hz), ECE measurements are most sensitive to k and C of the substrate, while at high frequency ($>3 \times 10^5$ Hz), C and d of SiN_x and $PbZr_{0.2}Ti_{0.8}O_3$ are the most important parameters.

VI. SUMMARY

In conclusion, we demonstrate a reliable technique for the direct measurement of the PEE and ECE in thin films using a microfabricated electrothermal test platform. Periodic heating via the top metal line results in localized heating of the ferroelectric and, in turn, in a flow of an external current which is separated into pyroelectric and thermally stimulated currents using frequency-domain phase-sensitive detection. Further, a wide-frequency-range measurement depicts the role of the secondary contribution to the PEE (approximately 30%) due to substrate clamping. The same device is used to measure the ECE where a high-frequency electric-field oscillation across the ferroelectric results in a temperature change which is sensed by the same top metal line now functioning as a resistance thermometer. Frequency-domain measurements allow the decoupling of Joule heating from the ECE. Using 1D heat-transport models, the thermal state of the heterostructure is characterized during the measurement of the PEE and the ECE to extract π and Σ.

ACKNOWLEDGMENTS

S. P. acknowledges support from the Army Research Office under Grant No. W911NF-14-1-0104. A. R. D. acknowledges support from the National Science Foundation under Grant No. CMMI-1434147. A. D. acknowledges support from the U.S. Department of Energy, Office of Science, Office of Basic Energy Sciences under Award No. DE-SC-0012375. L. W. M. acknowledges support from the National Science Foundation under Grant No. DMR-1451219. C. M. acknowledges funding from the Swiss National Science Foundation under Grant No. P2ELP2-152177.

APPENDIX: DESCRIPTION OF 1D HEAT-TRANSPORT MODELS

1. Pyroelectric effect

The full solution to the heat-diffusion equation for a heater-on-substrate geometry is solved in cylindrical coordinates. With the addition of thin films on top of the substrate, it is reasonable to approximate the heat transport through the films as one dimensional so long as the heater half-width b (5 μm) is greater than the total thickness of the film stack (<0.5 μm). An exact quantification of the error [38] in making this assumption caps the error in our model at less than 5%.

The steady, periodic solution to the one-dimensional heat-diffusion equation is well described by Carslaw and Jaeger [39], so many of the details will be skipped here. However, the transport matrix method for the practical application of the solution is described in detail. Starting from the analytical solution to the heat-diffusion equation, heat transport across a single domain can be written via vector multiplication as

$$\begin{bmatrix} \theta_d \\ q_d \end{bmatrix} = \begin{bmatrix} \cosh(\gamma d) & -\frac{1}{k\gamma}\sinh(\gamma d) \\ -k\gamma \sinh(\gamma d) & \cosh(\gamma d) \end{bmatrix} \begin{bmatrix} \theta_0 \\ q_0 \end{bmatrix} \tag{A1}$$

where $\gamma = \sqrt{j\omega/D}$, $j = \sqrt{-1}$, k is the material thermal conductivity, and d is the layer thickness. Recursive application of this transport matrix scheme can thus be used to describe a one-dimensional heat flow across several domains. That is,

$$\begin{bmatrix} \theta_N \\ q_N \end{bmatrix} = M_N M_{N-1} \ldots M_1 \begin{bmatrix} \theta_1 \\ q_1 \end{bmatrix}, \tag{A2}$$

where M_N is the transport matrix for the specified layer, containing the appropriate layer properties. Given any two of the temperatures or fluxes at either end of a domain, the other two can be found using this method.

In the PEE measurement scheme depicted [Fig. 3(c)], we measure the temperature amplitude (complex value) at the top surface of the stack, θ_H, using the 3-omega method, and the heat flux at the top surface, q_H, is just the ac power dissipated per unit area. These values are used to walk down the stack and thus determine the temperature amplitude at several positions within the stack. The key insight is to note that any single domain may be divided into an arbitrary number of subdomains, allowing for the calculation of desired values at any height within the stack. Note, also, that interfaces between layers are modeled as thin layers (approximately 1 nm) with a low thermal conductivity (1 $\mathrm{Wm^{-1}\ K^{-1}}$) and small heat capacity (10^5 $\mathrm{Jm^{-3}\ K^{-1}}$).

2. Electrocaloric effect

The 1D heat-transport model used for the PEE measurements can be extended to account for a heat source of finite thickness in the middle of a material stack in the case of the ECE measurements. A 1D model is valid here, because the heater (ferroelectric) half-width ($b = 5$ μm) is much greater than the total thickness of the film stack (<0.5 μm), and thus there is minimal lateral spreading within the substrate. Beginning with the transport matrices defined by Eq. (A1) for each layer in the stack, we can build up a formalism for the internal heat generation. Considering the stack [Fig. 4(c)], differential heat generated at an infinitesimal layer dz at height z diffuses up toward the surface of the stack and also into the substrate. This allows the stack to be divided into two subdomains: the upper (1) and lower (2) half of the stack, relative to height z within the ferroelectric. From these considerations we have three equations:

$$dq_{\mathrm{tot}} = dq_1 + dq_2, \tag{A3}$$

$$\begin{bmatrix} \theta_t \\ dq_t \end{bmatrix} = \begin{bmatrix} A_1 & B_1 \\ C_1 & D_1 \end{bmatrix} \begin{bmatrix} \theta_z \\ dq_{z_1} \end{bmatrix}, \tag{A4}$$

$$\begin{bmatrix} \theta_b \\ dq_b \end{bmatrix} = \begin{bmatrix} A_2 & B_2 \\ C_2 & D_2 \end{bmatrix} \begin{bmatrix} \theta_z \\ dq_{z_2} \end{bmatrix}, \tag{A5}$$

where the subscript t represents the properties of the bottom surface of the sensor, b the properties of the bottom surface of the substrate, z the properties of the ferroelectric layer at the prescribed height of interest, 1 the total transport matrix (i.e., the recursive multiplication of the M matrices for the relevant domains) for the upper domain, 2 the analogous transport matrix for the lower domain, and q_{tot} the total flux generated by the infinitesimal layer.

The fluxes at the top surface (adiabatic) and the bottom surface (semi-infinite) are zero. This allows us to write

$$C_1\theta_z + D_1 dq_{z_1} = 0, \tag{A6}$$

$$C_2\theta_z + D_2 dq_{z_2} = 0. \tag{A7}$$

Applying the conservation of flux, Eq. (A3), to these equations leads to

$$\theta_z = \left(\frac{-D_1 D_2}{C_1 D_2 + C_2 D_1}\right) dq_{\text{tot}}. \tag{A8}$$

The volumetric heat generated within the ferroelectric when exposed to an oscillating electric field, G, is defined by Eq. (13). Using Eq. (14), the temperature response at any plane in the ferroelectric can be calculated by

$$\theta_z = G \int_0^{d_{\text{FE}}} \left(\frac{-D_1 D_2}{C_1 D_2 + C_2 D_1}\right) dz. \tag{A9}$$

Equation (A9) can be applied to the top and bottom surfaces of the ferroelectric layer to determine the average temperature oscillation in the ferroelectric, $\theta_{\text{FE}} = \frac{1}{2}(\theta_{z=0} + \theta_{z=d_{\text{FE}}})$.

We can further extend this matrix formalism to determine an explicit expression for the temperature at the top surface of the stack (i.e., the temperature measured by the sensor). From Eqs. (A4) and (A6),

$$\theta_t = A_1\theta_z + B_1 dq_{z_1} = A_1\theta_z + B_1\left(-\frac{C_1}{D_1}\right)\theta_z. \tag{A10}$$

Finally, combining Eqs. (A9) and (A10),

$$\theta_t = G \int_0^{d_{\text{FE}}} \left(\frac{B_1 C_1 - A_1 D_1}{C_1 D_2 + C_2 D_1}\right) D_2 dz. \tag{A11}$$

We see in Eq. (A11) the complete expression used to relate the surface temperature measured by the heater line (θ_{sensor}) to Σ.

[1] M. E. Lines and A. M. Glass, *Principles and Applications of Ferroelectrics and Related Materials* (Oxford University, New York, 1977), p. 129.

[2] J. F. Scott, Electrocaloric materials, Annu. Rev. Mater. Res. **41**, 229 (2011).

[3] R. W. Whatmore, Pyroelectric devices and materials, Rep. Prog. Phys. **49**, 1335 (1986).

[4] A. Hadni, Applications of the pyroelectric effect, J. Phys. E **14**, 1233 (1981).

[5] A. Cuadras, M. Gasulla, and V. Ferrari, Thermal energy harvesting through pyroelectricity, Sens. Actuators A **158**, 132 (2010).

[6] Y. Yang, W. Guo, K. C. Pradel, G. Zhu, Y. Zhou, Y. Zhang, Y. Hu, L. Lin, and Z. L. Wang, Pyroelectric nanogenerators for harvesting thermoelectric energy, Nano Lett. **12**, 2833 (2012).

[7] A. Kitanovski, U. Plaznik, U. Tomc, and A. Poredo, Present and future caloric refrigeration and heat-pump technologies, Int. J. Refrig. **57**, 288 (2015).

[8] V. K. Pecharsky, J. Cui, and D. D. Johnson, (Magneto) caloric refrigeration: Is there light at the end of the tunnel?, Phil. Trans. R. Soc. A **374**, 20150305 (2016).

[9] A. G. Chynoweth, Dynamic method for measuring the pyroelectric effect with special reference to barium titanate, J. Appl. Phys. **27**, 78 (1956).

[10] S. B. Lang and F. Steckel, Method for the measurement of the pyroelectric coefficient, dc dielectric constant, and volume resistivity of a polar material, Rev. Sci. Instrum. **36**, 929 (1965).

[11] L. Pintilie, M. Alexe, I. Pintilie, and I. Boierasu, Thermally stimulated currents in $PbTiO_3$ thin films, Ferroelectrics **201**, 217 (1997).

[12] H. Okino, Y. Toyoda, M. Shimizu, T. Horiuchi, T. Shiosaki, and K. Matsushige, Thermally stimulated current and polarization fatigue in $Pb(Zr, Ti)O_3$ thin films, Jpn. J. Appl. Phys. **37**, 5137 (1998).

[13] I. Lubomirsky and O. Stafsudd, Invited review article: Practical guide for pyroelectric measurements, Rev. Sci. Instrum. **83**, 051101 (2012).

[14] L. E. Garn and E. J. Sharp, Use of lowfrequency sinusoidal temperature waves to separate pyroelectric currents from nonpyroelectric currents. Part I. Theory, J. Appl. Phys. **53**, 8974 (1982).

[15] E. J. Sharp and L. E. Garn, Use of lowfrequency sinusoidal temperature waves to separate pyroelectric currents from nonpyroelectric currents. Part II. Experiment, J. Appl. Phys. **53**, 8980 (1982).

[16] B. Bhatia, J. Karthik, T. Tong, D. G. Cahill, L. W. Martin, and W. P. King, Pyroelectric current measurements on $PbZr_{0.2}Ti_{0.8}O_3$, J. Appl. Phys. **112**, 104106 (2012).

[17] T. Tong, J. Karthik, L. W. Martin, and D. G. Cahill, Secondary effects in wide frequency range measurements of the pyroelectric coefficient of $Ba_{0.6}Sr_{0.4}TiO_3$, Phys. Rev. B **90**, 155423 (2014).

[18] S. Kar-Narayan, S. Crossley, X. Moya, V. Kovacova, J. Abergel, A. Bontempi, N. Baier, E. Defay, and N. D. Mathur, Direct electrocaloric measurements of a multilayer capacitor using scanning thermal microscopy and infra-red imaging, Appl. Phys. Lett. **102**, 032903 (2013).

[19] F. L. Goupil, A. Berenov, A. K Axelsson, M. Valant, and N. M. Alford, Direct and indirect electrocaloric measurements on ⟨001⟩-$PbMg_{1/3}Nb_{2/3}O_3$-30$PbTiO_3$ single crystals, J. Appl. Phys. **111**, 124109 (2012).

[20] X. Li, X. S Qian, H. Gu, X. Chen, S. G. Lu, M. Lin, F. Bateman, and Q. M. Zhang, Giant electrocaloric effect in ferroelectric poly(vinylidenefluoride-trifluoroethylene) copolymers near a first-order ferroelectric transition, Appl. Phys. Lett. **101**, 132903 (2012).

[21] L. W. Martin, Y. H Chu, and R. Ramesh, Advances in the growth and characterization of magnetic, ferroelectric, and multiferroic oxide thin films, Mater. Sci. Eng. R **68**, 89 (2010).

[22] D. G. Schlom, L. Q Chen, C. B Eom, K. M. Rabe, S. K. Streiffer, and J. M Triscone, Strain tuning of ferroelectric thin films, Annu. Rev. Mater. Res. **37**, 589 (2007).

[23] G. Chen, J. Zhao, S. Li, and L. Zhong, Origin of thickness dependent dc electrical breakdown in dielectrics, Appl. Phys. Lett. **100**, 222904 (2012).

[24] A. S. Mischenko, Q. Zhang, J. F. Scott, R. W. Whatmore, and N. D. Mathur, Giant electrocaloric effect in thin-film $PbZr_{0.95}Ti_{0.05}O_3$, Science **311**, 1270 (2006).

[25] A. S. Mischenko, Q. Zhang, R. W. Whatmore, J. F. Scott, and N. D. Mathur, Giant electrocaloric effect in the thin film relaxor ferroelectric $0.9PbMg_{13}Nb_{23}O_30.1PbTiO_3$ near room temperature, Appl. Phys. Lett. **89**, 242912 (2006).

[26] T. M. Correia, J. S. Young, R. W. Whatmore, J. F. Scott, N. D. Mathur, and Q. Zhang, Investigation of the electrocaloric effect in a $PbMg_{2/3}Nb_{1/3}O_3$-$PbTiO_3$ relaxor thin film, Appl. Phys. Lett. **95**, 182904 (2009).

[27] H. Chen, T. L Ren, X. M Wu, Y. Yang, and L. T Liu, Giant electrocaloric effect in lead-free thin film of strontium bismuth tantalite, Appl. Phys. Lett. **94**, 182902 (2009).

[28] Y. Liu, J. F. Scott, and B. Dkhil, Direct and indirect measurements on electrocaloric effect: Recent developments and perspectives, Appl. Phys. Rev. **3**, 031102 (2016).

[29] Xinyu Li, Sheng-Guo Lu, Xiang-Zhong Chen, Haiming Gu, Xiao-Shi Qian, and Q. M. Zhang, Pyroelectric and electrocaloric materials, J. Mater. Chem. C **1**, 23 (2013).

[30] B. Neese, B. Chu, S. G Lu, Y. Wang, E. Furman, and Q. M. Zhang, Large electrocaloric effect in ferroelectric polymers near room temperature, Science **321**, 821 (2008).

[31] B. Peng, H. Fan, and Q. Zhang, A giant electrocaloric effect in nanoscale antiferroelectric and ferroelectric phases coexisting in a relaxor $Pb_{0.8}Ba_{0.2}ZrO_3$ thin film at room temperature, Adv. Funct. Mater. **23**, 2987 (2013).

[32] T. Tong, J. Karthik, R. V. K. Mangalam, L. W. Martin, and D. G. Cahill, Reduction of the electrocaloric entropy change of ferroelectric $PbZr_{1-x}Ti_xO_3$ epitaxial layers due to an elastocaloric effect, Phys. Rev. B **90**, 094116 (2014).

[33] D. G. Cahill, M. Katiyar, and J. R. Abelson, Thermal conductivity of a-Si:H thin films, Phys. Rev. B **50**, 6077 (1994).

[34] S. Pandya, A. R. Damodaran, R. Xu, S. L Hsu, J. C. Agar, and L. W. Martin, Strain-induced growth instability and nanoscale surface patterning in perovskite thin films, Sci. Rep. **6**, 26075 (2016).

[35] J. Karthik, A. R. Damodaran, and L. W. Martin, Epitaxial ferroelectric heterostructures fabricated by selective area epitaxy of $SrRuO_3$ using an MgO mask, Adv. Mater. **24**, 1610 (2012).

[36] L. Pintilie, I. Vrejoiu, D. Hesse, and M. Alexe, The influence of the top-contact metal on the ferroelectric properties of epitaxial ferroelectric $Pb(Zr_{0.2}Ti_{0.8})O_3$ thin films, J. Appl. Phys. **104**, 114101 (2008).

[37] J. Karthik, A. R. Damodaran, and L. W. Martin, Effect of 90° Domain Walls on the Low-Field Permittivity of $PbZr_{0.2}Ti_{0.8}O_3$ Thin Films, Phys. Rev. Lett. **108**, 167601 (2012).

[38] C. Dames, *Measuring the Thermal Conductivity of Thin Films: 3 Omega and Related Electrothermal Methods*, Annu. Rev. Heat Transfer (Begell House, New York, 2013), Vol. 16, p. 7.

[39] J. C. Jaeger and H. S. Carslaw, *Conduction of Heat in Solids*, 2nd ed. (Clarendon, Oxford, 1959), p. 109.

[40] L. B. Schein, P. J. Cressman, and L. E. Cross, Electrostatic measurements of tertiary pyroelectricity in partially clamped $LiNbO_3$, Ferroelectrics **22**, 945 (1978).

[41] C. Dames and G. Chen, 1ω, 2ω, and 3ω methods for measurements of thermal properties, Rev. Sci. Instrum. **76**, 124902 (2005).

[42] L. Lu, W. Yi, and D. L. Zhang, 3ω method for specific heat and thermal conductivity measurements, Rev. Sci. Instrum. **72**, 2996 (2001).

[43] D. G. Cahill, M. Katiyar, and J. R. Abelson, Thermal conductivity of a-Si:H thin films, Phys. Rev. B **50**, 6077 (1994).

[44] D. G. Cahill, Thermal conductivity measurement from 30 to 750 K: The 3ω method, Rev. Sci. Instrum. **61**, 802 (1990); **73**, 3701(E) (2002).

[45] J. D. Zook and S. T. Liu, Pyroelectric effects in thin film, J. Appl. Phys. **49**, 4604 (1978).

[46] B. C. Gundrum, D. G. Cahill, and R. S. Averback, Thermal conductance of metal-metal interfaces, Phys. Rev. B **72**, 245426 (2005).